# SIMULATING SEISMIC WAVES IN EMBANKMENT DAMS FOR OPTICAL FIBRE DISTRIBUTED ACOUSTIC SENSING

REPORT 2023:944





# Simulating seismic waves in embankment dams for optical fibre Distributed Acoustic Sensing

JOHAN SUNDIN, ANNA STORK, ARIANA DAVID, SAM JOHANSSON

#### **Foreword**

The project was planned by Sam Johansson (HydroResearch). Johan Sundin (HydroResearch) set up the simulations and analysed results with inputs from Sam Johansson. The report was written together with Anna Stork and Ariana David (Silixa Ltd). The reference group consisted of Henrik Arver (Swedish Regulation Enterprises), Kerim Genel Waldenström (Vattenfall), Erik Nordström (Vattenfall), Petter Westerberg (Uniper), and Sezar Moustafa (Fortum).

The project has been carried out in the framework of the Energiforsk Dam Safety R&D Program with participation from the Swedish hydropower industry and Svenska kraftnät. The authors are responsible for the content.



# **Utökad sammanfattning**

Tillförlitliga övervakningsdata är avgörande för säker drift av alla dammtyper. Nya eller förbättrade övervakningsmetoder kan därför förbättra dammsäkerheten. Flera tekniker för övervakning av fyllningsdammar är idag tillgängliga. Exempel är läckage-, tryck-, rörelse- och temperaturmetoder samt elektriska och akustiska metoder. Denna studie behandlar akustiska metoder. De kan effektivt tillämpas på dammar som har optiska fibrer installerade genom distribuerade akustiska mätningar (Distributed Acoustic Sensing, DAS).

Akustiska metoder är baserade på seismiska vågors egenskaper, i synnerhet hastighet. De kan använda sig av volymvågor eller ytvågor. Ytvågor ger typiskt upphov till större markrörelser och dämpas mindre av geometrisk spridning än volymvågor. Det gör att ytvågor är lätta att uppmäta vid seismiska undersökningar. De kan genereras med hjälp av sprängladdningar, släggor, fallande vikter eller vibratorer. Seismiska vågor generas också av passiva källor som jordbävningar, havsvågor eller omgivande buller. De flesta studier som använder ytvågor baseras på Rayleighvågor.

Numeriska simuleringar kan ge nya insikter om övervakningsmetodernas bakomliggande fysikaliska mekanismer. Denna rapport presenterar resultat av simuleringar av ytvågutbredning i 12 m höga fyllningsdammar och kvantifierar skillnader mellan en intakt damm och en damm med en lokal defekt. Dammhöjden bestämdes genom en kompromiss mellan modellstorlek, som bestämmer beräkningstiden, och resultatens tillämpbarhet på stora dammar. Dammarna antas vara grundlagda på morän. Simuleringarna använder finita elementmetoden.

För dammarna med en simulerad defekt används ett område med högre porositet i tätkärnan. Där antas porositeten vara 0.35 i stället för 0.25. Områdena är horisontella cylindrar som går genom tätkärnan med radie 1, 2 eller 4 m. Sådana defekter liknar skador orsakade av inre erosion. Vattenflöden har där tagit bort mindre partiklar vilket ökar porositeten. Eftersom partiklarna har en högre densitet än vattnet får defekterna en lägre densitet, vilket leder till en högre våghastighet. Sådana avvikelser kan uppmätas med DAS. Storleken på avvikelsen bestäms med de numeriska simuleringarna.

En fyllningsdamm utgörs av jord (samt sten), vatten och luft. Grundvattennivån i dammen bestäms av magasinets nivå och vattennivån nedströms dammen. Dammens material är mättat under och omättat över grundvattennivån. Den effektiva densiteten hos materialet varierar på motsvarande sätt. Andra parametrar som skjuv- och kompressionsmodul kan också variera i dammen. Det har dock antagits att dessa variationer är sekundera för defekters påverkan på våghastigheten och de har därför exkluderats.

Dammens vattenmättnad beräknas genom att lösa Richards ekvation, vilket ger den effektiva materialdensiteten. De seismiska simuleringarna beskriver dammen som ett linjärt elastiskt medium. Materialets dämpning av vågorna beskrivs med Rayleighs dämpningsmodell. Ytvågor exciteras genom en harmonisk vertikal kraft som angriper vid dammkrönets kant. Vågornas fashastighet beräknas därefter



utifrån frekvensen och den rumsliga derivatan av vågfasen längs tätkärnans krön. Fiberoptiska kablar tänkta för akustikmätningar kan placeras där.

Vattennivån uppströms och nedströms dammen är 7 respektive 2 m över grunden. Kapillarkrafter beaktas genom van Genuchtens vattenbindningsmodell. Hastigheterna som uppkommer är i dammen är typiskt kring 1–10  $\mu$ m/s. Medelflödet genom dammen utan defekter beräknas till ca 14 ml/(s·m). Det är ett representativt värde för svenska dammar. Flödet ökar om dammen har en defekt. För dammen den största defekten (med radie 4 m) är flödet ca 200 ml/(s·m).

Om buller används för att excitera ytvågor begränsas vågornas frekvenser av bullrets frekvensinnehåll. I industriella miljöer dominerar vanligtvis en viss frekvens, till exempel om en generator körs i närheten. Vågor med högre frekvenser ger bättre upplösning, men dämpas snabbt. En tidigare studie baserad på mätningar vid Älvkarlebys testdamm använde vågfrekvenser i intervallen 15–27 och 10–25 Hz. De numeriska simuleringarna använder frekvensen 15 Hz.

Vågorna som exciteras ses som områden med växlande hög och låg förskjutningsamplitud. Storleken på den vertikala förskjutningen är generellt större än den längs med dammen. Förskjutningen längs med dammen ändrar tecken vid ett djup på ca 1 m. Teckenändringen överensstämmer med teorin för Rayleighvågor. Förskjutningens avtagande med djupet är dock något avvikande, då förskjutningen är stor även vid djupet av en våglängd. Avtagandet varierar också till viss del med avståndet till källan. Simuleringar med defekten på olika ställen längs dammen visar dock inte på något markant ändrat beteende, även om storleken på defektens våghastighetsförändring varierar något.

Vågornas amplitud avtar nästan monotont längs tätkärnans krön med avståndet till källan. Amplituden påverkas inte nämnvärt av defekterna. Fasen beror i det närmaste linjärt på dammsektion. Defekter ger dock upphov till en viss fasförskjutning, vilket tydligast syns för den största defekten. Fasändringen kan uttryckas som en förändring av våghastigheten kring defekten, eftersom våghastigheten beräknas från den rumsliga derivatan av fasen.

För både intakta och defekta dammar är våghastigheten ca 100 m/s, vilket väl överensstämmer med teoretiska värden. Simuleringarna visar att förändringen i utbredningshastigheten vid defekterna är kring 0.5–3%. Även det stämmer med vad som kan förväntas från teoretiska förutsägelser utifrån ändringen i porositet. Den uppmätta avvikelsen är dock något mindre än det teoretiska värdet, vilket kan förväntas då defekterna bara upptar en mindre del av dammarnas tvärsnitt. Avvikelsen ökar också med defektens storlek.

Simuleringarna visar att hastigheten inte bara påverkas av förändringar i direkt anslutning till mätpunkten. Precisionen hos mätinstrumenten som används för DAS förmodas bestämma den minsta uppmätbara hastighetsförändringen, och således vilka defekter som kan detekteras. En hastighetsförändring på 1% är tillräckligt stor för att registreras av moderna instrument.

Hastighetsfluktuationer på ca 5 m/s syns även för en intakt damm. I närheten till källan har ytvågorna inte helt utvecklats, så hastigheten kan inte förväntas vara konstant där. Fluktuationer syns dock även längre bort på dammen. Simuleringar



av en längre damm indikerar att dammens ändrandvillkor är involverade i fluktuationernas uppkomst. Deras storlek minskade även då grundens material ändrades till berg. Påverkan från dammens ändar och grunden, till exempel genom interferens med reflekterade vågor, är i praktiken ofrånkomligt på verkliga dammar.

Defekterna ger också upphov till mindre hastighetsavvikelser längre bort från dem. Om defekterna förväntas finnas vid de största avvikelserna skulle de generellt bli korrekt identifierade. Om dammen har ett okänt antal defekter så skulle mindre defekter dock kunna vara svåra att upptäcka. De är möjligt att fluktuationerna längre bort från defekterna minskar om materialparametrar ändras gradvis och inte abrupt.

Magasinsnivån påverkar den uppmätta våghastigheten endast marginellt. En lägre magasinsnivå tenderar att ge något högre hastigheter, vilket återspeglar minskningen i densitet. Vattennivåer kan dock påverka skjuvmodulen genom kapillär- och spänningseffekter, vilka här har utelämnats. Förutom att minska fluktuationer i hastigheten uppvisar simuleringar med ett grundmaterial av berg en något mindre hastighetsavvikelse vid defekten.

Vi tror att akustiska metoder, och i synnerhet ytvågsmetoder, skulle kunna komplettera mer etablerade övervakningstekniker som temperaturmätningar i optiska fiber. Eftersom optiska kablar installerade i många dammar kan registrera seismiska vågor kan akustiska metoder tillämpas utan större installationskostnader. Potentialen hos fiberoptiska metoder är också ett starkt argument för att installera fiberoptiska kablar vid konstruktion av nya dammar.

Som en fortsättning på denna studie skulle vågor med olika frekvenser och med defekter på olika djup kunna simuleras. Anfang och en större del av grunden kan också tas med i geometrin. Simuleringar kan också utföras på verkliga dammar, som Älvkarlebys testdamm. Det skulle möjliggöra en direkt jämförelse mellan numeriska och uppmätta resultat.

**Nyckelord:** Distribuerade akustiska mätningar, interferometrisk analys av omgivningsljud, seismisk hastighet, fyllningsdammar, detektion av skador, inre erosion.



# **Summary**

Adequate monitoring data is essential for safe dam operation for all dam types. New or improved monitoring methods are thus of great importance in advancing dam safety. Several embankment dam monitoring techniques are available today, such as seepage, pressure, movement, temperature, electrical, and acoustic methods. This study considers acoustic methods. They can effectively be applied in dams with optical fibres installed using Distributed Acoustic Sensing.

Numerical simulations can provide new insights into the physical mechanisms behind monitoring techniques. Acoustic methods are based on the properties of seismic waves, especially velocity. Results of Finite Element Method simulations of seismic wave propagation in a 12 m tall embankment dam are presented in this report. A literature review on seismic waves in porous media is also provided.

The simulation setups include regions of higher porosity in the dam core. The porosity at these defects is assumed to be 0.35 instead of 0.25. Such defects resemble damages caused by internal erosion. Water flow has there removed fines, increasing the porosity. Since the solid material has a higher density than water, these regions have a lower density than surrounding media, leading to a higher seismic velocity.

The liquid volume fraction is found by solving Richards' equation, giving the effective material density used in the seismic simulations. The seismic simulations assume the dam to be a linear elastic medium. A harmonic vertical forcing located at the dam edge is used to excite surface waves. The wave phase velocity can be determined by the source frequency and the spatial derivative of the wave phase computed along the core crest.

The simulations show that the change in seismic velocity due to defects is on the order of 1%. The magnitude depends on the defect size. The simulations also illustrate that the velocity is sensitive to changes in dam properties not only in the direct vicinity of the measurement point. Upstream water level and dam foundation material are seen to only influence the seismic velocity marginally. However, water levels could influence the shear modulus through capillary and stress effects which have been neglected here.

The velocity change of 1% is large enough to be registered by state-of-the-art instruments. We believe that acoustic methods and especially surface wave methods could complement more established monitoring techniques such as temperature measurements. Given that optical cables installed in many dams can register seismic waves, acoustic methods could be applied without significant installation costs.

**Keywords:** Distributed Acoustic Sensing, Ambient Noise Interferometry, seismic velocity, embankment dams, detection of defects, internal erosion.



# List of content

L	Introd	luction				
2	Object	tives	11			
3	Seism	ic velocities in porous media	12			
	3.1	Wave propagation modes	12			
	3.2	Models of material properties	13			
1	Dam s	simulation setup				
	4.1	Geometry and simulation parameters	16			
	4.2	Governing equations and numerical method	17			
		4.2.1 Richards' equation	18			
		4.2.2 Linear elastic medium	18			
		4.2.3 Boundary conditions	19			
	4.3	Mesh	19			
	4.4	Defects	20			
5	Result	ts	22			
	5.1	Volume fraction, flow, and pressure fields	22			
	5.2	Static load	24			
	5.3	Frequency response of harmonic perturbations				
		5.3.1 Dam without defects	25			
		5.3.2 Defects' effect on phase velocity	28			
5	Conclu	sions and outlook 3:				
7	Refere	ences	32			
Appendix A:		Mesh sensitivity study	34			
Appendix B:		Foundation size sensitivity study				
Appendix C:		Effects of defect spanwise location	37			
Appendix D:		Water level dependency	39			
Appendix E:		Dam on rock foundation				



#### 1 Introduction

Safe dam operation is dependent on comprehensive monitoring data. Monitoring is used to detect defects in a dam before they develop to threaten the dam's integrity. Surveillance method development is therefore central to the ongoing work of improving dam safety. Different techniques can today be used for embankment dam monitoring, such as seepage, pressure, movement, temperature, electrical, and acoustic methods.

Acoustic methods are based on the propagation of elastic waves. They include seismic refraction and reflection, surface wave imaging, echo sounding or sonar measurements, and seepage sound measurements (Sjödahl, Johansson, & Dahlin, 2019). Refraction of seismic waves is caused by velocity variations with rock properties. A change in rock property can also cause reflections. Refraction and reflection methods make use of body wave recordings. Surface waves travel along the Earth's surface and are the focus of the current study.

Surface waves typically cause larger amplitude ground motions than body waves and are less dampened by geometric spreading. These properties make surface waves easily accessible in seismic surveys (Socco, Foti, & Boiero, 2010).

Acquired surface wave travel-time data can be used to determine wave phase velocities and dispersion relations. By solving an inverse problem, the dispersion relation gives information about material parameters at different depths (such as the shear-wave velocity) but may require assumptions of other material parameters (e.g. density and Poisson's ratio) (Sjödahl, Johansson, & Dahlin, 2019). Since the 1990s, data acquisition has typically been performed with multiple receivers (Socco, Foti, & Boiero, 2010). One technique to obtain velocities for the near-surface is called Multichannel Analysis of Surface Waves, MASW (Park, Miller, & Xia, 1999).

Surface waves can be generated by explosives, weight drops, sledgehammers, or seismic vibrators (Sjödahl, Johansson, & Dahlin, 2019). It is also possible to excite surface wave using passive sources such as earthquakes, ocean noise, or anthropogenic sounds. Information can then be extracted from recorded signals using Ambient Noise Interferometry, ANI (Johansson, Beaupretre, Boue, & Stork, 2021).

Optical fibres were introduced in dam monitoring in Sweden 1998 and is now used in about 90 dams (Johansson & Sjödahl, 2017). They allow the measurement of thousands of points simultaneously and have been used mostly for temperature and strain measurements (Parker, Farhadiroushan, Handerek, & Roger, 1997; Johansson & Watley, 2006). However, they can also be used to measure the amplitude, frequency, and phase of acoustic waves (Parker, Shatalin, & Farhadiroushan, 2014). The measuring of acoustic signals with optical fibres is called Distributed Acoustic Sensing (DAS). DAS offers a much wider coverage in MASW surveys than traditionally used point receivers. It also simplifies the implementation of acoustic methods for dam monitoring, since many dams have optical fibres already installed.



This report describes the setup and evaluation of seismic and flow simulations of an embankment dam with defects. The simulations have been performed with COMSOL Multiphysics®.

The project is a continuation of and complements two earlier projects funded by Energiforsk (Johansson, Beaupretre, Boue, & Stork, 2021; Johansson, Beaupretre, Mordet, & Stork, 2022). In these projects, DAS-ANI surveys were carried out on a dam with built-in defects in Älvkarleby, Sweden. They also included some preliminary numerical modelling. In contrast to these experimental investigations, the behaviour of the seismic waves can be fully observed in the current simulations. The simulation setup can also be used to determine the sensitivity of the results to variations in model parameters such as defect size.



# 2 Objectives

The objectives are summarised below.

- Perform a literature study about seismic velocity in porous media in the context of dam monitoring.
- Perform seismic simulations of dams with and without defects based on the modelling used by Johansson et al. (2022) and the literature study.
- Analyse the simulation results and their dependency on parameters describing the defects.

In the literature study we collect information on acoustic theory and evaluate how acoustic methods can be applied for dam monitoring, especially based on DAS measurements. Experience of using acoustic methods on dams is limited and there are uncertainties in dam material or basement rock properties. This step is thus important for the further development of this method for dam monitoring.

A Finite Element Method (FEM) is used for the seismic modelling, where several theories can be tested. Of special interest is to study the impact of the dam geometry that differs from most other applications of acoustic methods, especially those using surface-wave data recorded with DAS in embankment dams.

The simulations also include computations of seepage flow and saturation, which is of importance for the seismic velocity in the dam and its assumed defects. From the results, it is possible to extract local changes in wave amplitudes and phases. We are then able to quantify the wave-velocity change due to defects caused by internal erosion

With an appropriate FEM-model established, we carry out sensitivity analyses of some relevant parameters. The results provide valuable input for decision-making to apply acoustic methods for a specific investigation or monitoring situation.



# 3 Seismic velocities in porous media

In this section, we give an overview of different types of waves and how their velocities can be estimated. We also describe how the velocities depend on material parameters relevant for dam applications.

#### 3.1 WAVE PROPAGATION MODES

In an infinite elastic medium, compressional (or primary, P-) wave and shear (secondary, S-) waves propagate. Surface waves, such as Rayleigh (R-) waves, propagate near the boundary of a half-space. The different wave types are distinguished by the motion of material particles. P- and S-waves have particle motions parallel and transverse to the direction of wave propagation, respectively. R-waves have elliptical (i.e. both parallel and transverse) particle motions (Santamarina, Klein, & Fam, 2001, p. 193). Surface waves properties are central to surface wave methods whereas P- and S-wave properties are of interest in refraction and reflection methods. P-waves travels faster than S-waves and R-waves are slower than S-waves.

P-wave and S-wave phase velocities can be expressed by

$$V_P = \sqrt{\frac{K + ^4/_3 \mu}{\rho}} \text{ and } V_S = \sqrt{\frac{\mu}{\rho}},$$
 (1), (2)

respectively, where K is the bulk modulus,  $\mu$  is the shear modulus and  $\rho$  is the density (Santamarina, Klein, & Fam, 2001, p. 192). Since  $K + 4\mu/3 > \mu$ , the P-wave velocity is higher than the S-wave velocity. The R-wave velocity  $V_R$  is slightly lower than  $V_S$ . Several approximate expressions for  $V_R$  exist, with one being (Malischewsky, 2005)

$$V_R = V_S(0.874 + 0.196\nu - 0.043\nu^2 - 0.055\nu^3),$$
 (3)

where v is Poisson's ratio.

Other surface wave types exist. If the half-space has layers, reflections can generate so-called Love waves. This wave type only occurs if the top layer has lower phase velocity than the second layer (Richart, Hall, & Woods, 1970, p. 100). However, most surface wave analyses use R-waves (Socco, Foti, & Boiero, 2010). A fibre-optic cable along a dam crest is most sensitive to R-waves travelling along the dam inline with the cable. Seismic waves travelling through a medium can also be scattered by inhomogeneities. The resulting waves are called coda waves, which can be used in seismic surveys (Johansson, Beaupretre, Boue, & Stork, 2021; Johansson, Beaupretre, Mordet, & Stork, 2022).

For high frequencies, inertial effects of the fluids become important, and the wave velocity relations presented here lose validity (Santamarina, Klein, & Fam, 2001, p. 238). A theory that accounts for high frequency effects has been developed by Biot (1956a; 1956b). It predicts two kinds of P-waves in saturated porous materials: the standard (fast) wave and another slow wave. Both P-wave velocities and the S-



wave velocity increase with frequency. High frequency effects can be necessary to account for around and above the characteristic frequency

$$f_c = \frac{\varphi \eta}{2\pi \rho_f \kappa_s},\tag{4}$$

where  $\varphi$  is the porosity,  $\eta$  is the fluid dynamic viscosity,  $\rho_f$  is the fluid density, and  $\kappa_s$  is the permeability (Santamarina, Klein, & Fam, 2001, p. 239). For an order of magnitude estimation of  $f_c$ , we assume the fluid to be water ( $\rho_f = \rho_w = 1000 \text{ kg/m}^3$  and  $\eta = \eta_w = 1.0 \cdot 10^{-3} \text{ Pas}$ ),  $\varphi = 0.25$ , and  $\kappa_s = 2 \cdot 10^{-10} \text{ m}^2$ , giving  $f_c = 200 \text{ Hz}$ . Relevant frequencies in this study are about an order of magnitude smaller (Section 5.3). Therefore, we do not consider Biot's theory here.

#### 3.2 MODELS OF MATERIAL PROPERTIES

An embankment dam constitutes soils with different properties, water, and air. The dam water table depends on the reservoir and downstream (DS) water levels, which generally vary with time. The soil is saturated below and unsaturated above the water table. The effective material density varies correspondingly. In general, the bulk and shear moduli also vary inside the dam. Water saturation affects the bulk modulus as it is a function of the solid particle, water, and air compressibility and their volume fractions. The shear modulus is influenced by capillary forces and the imposed stress.

The effective density of the dam can be expressed by

$$\rho = (1 - \varphi)\rho_s + \theta\rho_w, \tag{5}$$

where  $\rho_s$  is the solid (mass) density and  $\theta$  is the liquid volume fraction (Richart, Hall, & Woods, 1970, p. 130). This expression neglects the air density. The liquid volume fraction can attain values  $\theta_{res} \le \theta \le \theta_{sat}$ , where  $\theta_{res}$  is the residual volume fraction and  $\theta_{sat} = \varphi$  is the saturated liquid volume fraction. When water replaces air, the density increases. Correspondingly, the wave velocities decrease.

The effective bulk modulus of the dam is determined by the bulk moduli of the water, air, and solid particles. The bulk modulus is the inverse of the compressibility. The pore fluid bulk modulus  $K_f$  is

$$\frac{1}{K_f} = \frac{\theta}{\varphi} \frac{1}{K_W} + \left(1 - \frac{\theta}{\varphi}\right) \frac{1}{K_{\alpha'}} \tag{6}$$

where  $K_w$  = 2.2 GPa and  $K_a$  = 140 kPa are the water and air bulk moduli, respectively (Santamarina, Klein, & Fam, 2001, p. 235). Even minor amounts of air can have a large impact on  $K_f$ .

If the soil is considered a water-air-solid particle suspension, its effective bulk modulus  $K_{sus}$  is given by

$$\frac{1}{K_{Sus}} = \frac{1-\varphi}{K_{Sp}} + \frac{\varphi}{K_f},\tag{7}$$

where  $K_{sp}$  is the bulk modulus of the solid particles (Santamarina, Klein, & Fam, 2001, p. 235). However, the solid particles are generally connected, forming a solid



skeleton with bulk modulus  $K_{ss}$ . Typically,  $K_{ss} \ll K_{sp}$ . The bulk modulus can be modelled by

$$K = K_{sus} + K_{ss}. (8)$$

A slightly more general equation, accounting for volumetric changes, is usually attributed to Gassmann (1951). For saturated soils, K is mainly determined by  $K_f$  (Cho & Santamarina, 2001, p. 251). As  $\theta$  is reduced,  $K \approx K_{ss}$ .

The shear modulus, on the other hand, can be assumed to only depend on the skeleton shear modulus (Santamarina, Klein, & Fam, 2001, p. 237). However, the shear modulus is affected by capillary forces, altering the inter-particle contacts. Therefore, as  $\theta$  varies in the unsaturated zone of the dam,  $\mu$  also changes. The matter is complicated, with many processes involved. For example, the formation of continuous gas and liquid phase paths is dependent on whether the soil is being wetted or is drying, i.e. there are hysteresis effects. During drying, fines may form buttresses and salt crystals may develop between larger grains, increasing the skeleton stiffness (Santamarina, Klein, & Fam, 2001, p. 171).

Studies have indicated significant changes in  $\mu$  with varying saturation for different particle grain sizes and types, e.g. glass beads, kaolinite, granite powder, sand, silt, clay, and claystone (Cho & Santamarina, 2001; Dong & Lu, 2016). It should be noted that  $\rho$  decreases and  $\mu$  tends to increase with decreasing  $\theta$  (even if a maximum may exist for  $\mu$ ). Thus, they both contribute to increasing  $V_S$  as the saturation level is reduced.

The shear modulus is also affected by the effective load on the solid skeleton. A concept of effective stress, being the stress with the pore fluid pressure accounted for, has therefore been developed. The idea behind this concept is that the solid skeleton carries the stress not taken by the fluid (Santamarina, Klein, & Fam, 2001, p. 82). For saturated soils, Terzaghi (1936) suggested an effective stress

$$\sigma' = \sigma_c - p_w I, \tag{9}$$

where  $\sigma_{\mathcal{L}}$  is the confining stress,  $p_w$  is the pressure in the water, and I is the identity matrix. Accounting for capillary forces in unsaturated soil, Bishop (1960) proposed

$$\sigma' = \sigma_c - p_a I + \chi (p_a - p_w) I, \tag{10}$$

where  $p_a$  is the air pressure,  $\chi$  varies from  $\chi = 0$  in dry to  $\chi \approx 1$  in saturated soils (Mitchell & Soga, 2005, p. 180). The influence of the effective stress level on the shear velocity can be significant. In general, the shear velocity increases with increasing load. For dry or saturated soils, the effective stress dependency of  $\mu$  is usually taken to be a power law (Mitchell & Soga, 2005, pp. 447–450). The bulk modulus can be modelled similarly.

The modelling of  $\mu$  in soils with varying saturation and stress differ. Constitutive variables of proposed relations include stress, effective stress, saturation, and air and water pressure difference (i.e. suction or capillary pressure), in different combinations (Ng, Zhou, & Chiu, 2020). However, defects are assumed not to primarily give rise to changes in effective stress. Also, defects can be expected to be found in the saturated part of the dam. Therefore, in the absence of generally



accepted models and to simplify the analysis, we have neglected the stress and saturation dependencies of  $\mu$  in this study.

Another parameter that can affect  $\mu$  is the temperature (freezing included). The temperature influences capillary forces since surface tension and soil-water contact angles are temperature dependent (Vahedifard, Thota, Cao, Samarakoon, & McCartney, 2020). It can also affect the seepage flow rate since water viscosity and density vary with temperature.

A comprehensive list of parameters with potential influence on the shear modulus was given by Hardin & Back (1968), of which the most relevant have been discussed here.



# 4 Dam simulation setup

The reservoir and downstream water levels and dam material properties determine the water content in the dam. The water content and flow velocities have been computed using COMSOL Multiphysics® (version 6.1), solving Richards' equation (Johansson, Beaupretre, Mordet, & Stork, 2022). With the water content known, seismic wave propagation has been investigated using the same software.

COMSOL Multiphysics® enables the simulation of sound wave propagation in fluids and solids. Assuming the dam to effectively be a linear elastic solid, we have computed the displacement field of the seismic waves. This study considers a harmonic noise source. Effective material properties have been specified by the bulk modulus, shear modulus, and density. The density was computed through equation (5), whereas the other parameters were constants.

#### 4.1 GEOMETRY AND SIMULATION PARAMETERS

The geometry of the considered dam model is shown in Figure 1. It was constructed by combining hexahedrons, consisting of a core, filters, support fills, and a foundation. The dam had a crest length of 100 m and a height of 12 m. This length was selected as it allows waves to develop while the model remains small enough to simulate. For the same reason, the height could not be too large. The current value is believed to give a good compromise between model size and the applicability of the results to large dams. The slope of the support fills was 2, determining the dam width.

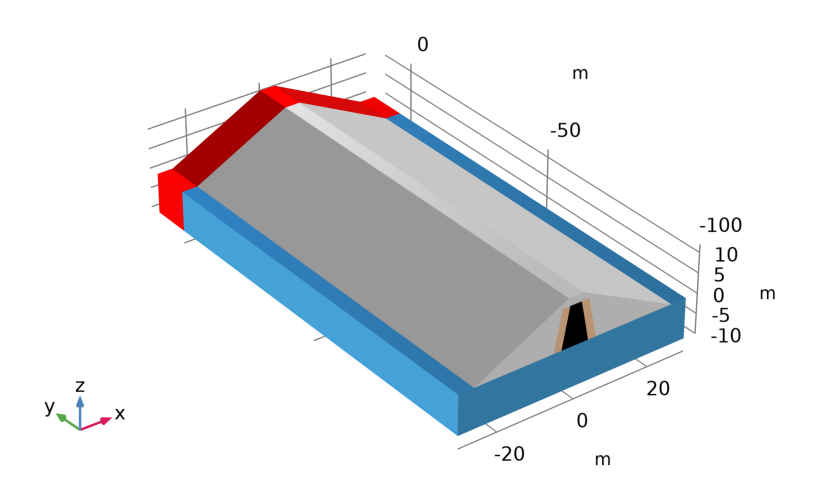


Figure 1 Illustration of the dam geometry, including the core, filters, support fill, foundation, and PML (black, brown, grey, blue, and red, respectively).

The acoustics simulations required an extra region at the end of the dam of 10 m. This region is a so-called Perfectly Matched Layer (PML, Section 4.2.3), treated as a regular part of the dam in the flow (and static load) simulations. The core and filters were assumed to be 10 m high and the foundation 10 m deep. The fill above



the core crest was 2 m high. The streamwise, dam section, and vertical coordinates are x, y, and z, respectively.

The core and the foundation were considered to consist of one material, corresponding to a dam placed on till. The filters were made of a second material and the fills of a third. The porosity and the permeability differed between the materials and are given in Table 1. The solid density was assumed to be  $\rho_s$  = 2700 kg/m<sup>3</sup>.

Table 1 Porosity and permeability at saturation ( $\varphi$  and  $\kappa_s$ , respectively) of dam materials and the defect region. Theoretical wave velocities are also given.

	Core	Filter	Fill	Defect
φ	0.25	0.25	0.35	0.35
$\kappa_s$ [m <sup>2</sup> ]	2.10-13	2·10-10	1.10-9	2·10-10
$Vs$ [m/s], $\theta = 0$	107	107	114	114
$Vs$ [m/s], $\theta = \varphi$	101	101	105	105
$V_R$ [m/s], $\theta = 0$	100	100	108	108
$V_R$ [m/s], $\theta$ = $\varphi$	95	95	98	98

We use the same effective shear modulus as Johansson et al. (2022),  $\mu$  = 23 MPa. The bulk modulus was set to K = 100 MPa in the simulations. The surface waves are expected to mostly dependent on the shear wave velocity and thereby the shear modulus. The Poisson's ratio becomes (COMSOL AB, 2022a, p. 427)

$$\nu = \frac{1}{2} \left( 1 - \frac{3\mu}{3K + \mu} \right) = 0.39. \tag{11}$$

Also, Young's modulus is

$$E = \frac{9K\mu}{3K+\mu} = 64 \text{ MPa.}$$
 (12)

By Equation (3),  $V_R = 0.94V_S$ . A higher (lower) bulk modulus would increase (decrease)  $\nu$ , resulting in a higher (lower)  $V_R$ . For K=0 and  $K\to\infty$  (i.e.  $\nu=-1$  and  $\nu=0.5$ ), Equation (3) gives  $V_R=0.69V_S$  and  $V_R=0.95V_S$ , respectively. Especially the upper limit corresponds to a relatively minor change compared to the current value. Table 1 includes wave velocities predicted by Equations (2) and (3) for the considered material parameters. They were computed using the limiting values  $\theta=0$  and  $\varphi$  (Section 4.2.1).

#### 4.2 GOVERNING EQUATIONS AND NUMERICAL METHOD

In this section, we give a summary of the governing equations and boundary conditions for the flow and seismic simulations.

For the discretisation of the pressure in Richards' equation, we used quadratic Lagrange shape functions (COMSOL AB, 2022b, p. 139). To discretise the displacement field, we used cubic serendipity shape functions (COMSOL AB, 2022a, p. 837). The reason for using the higher-order discretisation for the displacement field was to reduce errors when computing the wave velocity (by equation (21) below).



#### 4.2.1 Richards' equation

Richards' equation for the steady-state pressure is (COMSOL AB, 2022b, p. 132)

$$\nabla \cdot \rho_w \left( -\frac{\kappa_r \kappa_s}{\eta_w} (\nabla p_w - \rho_w \boldsymbol{g}) \right) = 0, \tag{13}$$

where  $\kappa_r$  is the relative permeability and g is the gravitational acceleration vector. The Darcy's fluid velocity field (i.e. specific discharge) is computed from the pressure simply as

$$\boldsymbol{u} = -\frac{\kappa_r \kappa_s}{\eta_w} (\nabla p_w - \rho_w \boldsymbol{g}). \tag{14}$$

We used the COMSOL® implementation of the van Genuchten (1980) retention model to compute the volume fraction and  $\kappa_r$ . The volume fraction is

$$\theta = \theta_{res} + S(\theta_{sat} - \theta_{res}), \text{ with } S = \begin{cases} \frac{1}{(1 + |\alpha H|^n)^m}, & H < 0\\ 1, & H \ge 0 \end{cases}$$
 (15)

where *S* is effective saturation,  $H = p_w/(\rho_w g)$  is the pressure head (for  $p_a = 0$  and g being the norm of g), n and  $\alpha$  are (positive) constants, and m = 1 - 1/n. The relative permeability is defined by

$$\kappa_r = S^l \left[ 1 - \left( 1 - S^{\frac{1}{m}} \right)^m \right]^2. \tag{16}$$

The residual volume fraction  $\theta_{res}$  was set to zero. Hence,  $S = \theta/\varphi$ . The other parameters were chosen as  $\alpha = 1.0$  1/m, n = 2.0, and  $l = \frac{1}{2}$ , which are the default COMSOL Multiphysics® values (COMSOL AB, 2022b, p. 111). They are suitable for materials with low permeability.

#### 4.2.2 Linear elastic medium

The displacement vector  $\mathbf{s} = (s_x, s_y, s_z)$  of the material is described by (COMSOL AB, 2022a, p. 420)

$$\rho \frac{\partial^2 \mathbf{s}}{\partial t^2} = \nabla \cdot \mathbf{\sigma} + \rho \mathbf{g},\tag{17}$$

where  $\rho$  is the effective density (5), t is time,  $\sigma$  is the (Cauchy) stress tensor, and damping is neglected. We assume a linear elastic material, such that the stress by Hook's law is (neglecting geometric nonlinearities)

$$\sigma = C: \varepsilon \text{ with } \varepsilon = \frac{1}{2} (\nabla s + (\nabla s)^T),$$
 (18)

where  $\epsilon$  is the strain tensor, C is the fourth-order elasticity tensor, and : indicates the double-dot tensor product (COMSOL AB, 2022a, pp. 389, 425). Assuming an isotropic material, the elasticity tensor is completely defined by K and  $\mu$  (COMSOL AB, 2022a, p. 426).

Equations (17) and (18) are linear and material parameters are assumed to not depend on the material stress. Therefore, we solve for displacements caused by static forces and harmonic forces separately.



To account for material damping, we use the Rayleigh damping model. The Rayleigh mass and stiffness damping parameters were set to  $\alpha_{\text{dM}} = 0.8 \text{ 1/s}$  and  $\beta_{\text{dK}} = 4 \cdot 10^{-4} \text{ s}$ , respectively. These values are approximately those found by Ju & Ni (2007). They give the damping ratio (COMSOL AB, 2022a, p. 184)

$$\zeta = \frac{1}{2} \left( \beta_{\text{dK}} 2\pi f + \frac{\alpha_{\text{dM}}}{2\pi f} \right) = 0.023,$$
 (19)

for a frequency f = 15 Hz.

#### 4.2.3 Boundary conditions

The water levels were specified at the upstream (US) and DS side. Having the foundation top at z = 0 m, the US and DS water levels were  $z_{WL,US} = 7$  m and  $z_{WL,DS} = 2$  m, respectively.

For the flow simulations, we set an inlet condition on the US side of the dam at the bottom of the reservoir and up to *zwL,us*. Similarly, an outlet condition was set on the DS side up to *zwL,Ds*. These conditions specified the boundary pressure to be equal to the hydrostatic pressure (i.e. linearly increasing up to the water levels). All other outer boundaries were set to have zero normal flow (i.e. being impermeable).

In the static load simulations, the water was accounted for by prescribing the hydrostatic pressure as for the flow simulations. The remaining part of the upper side of the dam could move without constraints. To have a net zero force imposed on the dam, the bottom of the foundation was set to have zero displacement. The remaining sides were restricted to move only in the surface plane (roller conditions).

In the harmonic noise simulations, a 10 m region at the end of the dam was set to be a PML (Figure 1). This region acts as a non-reflecting infinite domain (COMSOL AB, 2022c, s. 234). The bottom, US, and DS sides of the foundation were set to be regular low-reflecting boundaries. The upper side of the dam moved without constraints, whereas the remaining end of the dam had a roller condition.

#### 4.3 MESH

The mesh was constructed with unstructured tetrahedral elements, using the built-in COMSOL Multiphysics® mesh generator. However, the PML region had a structured (swept) mesh, consisting of eight element layers. The mesh is shown in Figure 2.

The wavelength is  $\lambda = V/f$ , where V is the wave phase velocity and f the frequency. The theoretical wavelengths were used as references when designing the mesh element sizes, as the mesh needs to be fine enough to resolve waves with the smallest wavelength. The slowest waves have the smallest wavelengths. According to Equations (1), (2), and Table 1, the slowest waves are found in the regions of highest density, corresponding to fully saturated core, foundation, and filter regions. Looking at S-waves and f = 15 Hz, the smallest wave wavelength was computed to  $\lambda_{S,min} = Vs/f = (101 \text{ m/s})/f = 6.7 \text{ m}$ .



We use a maximum element size of  $\lambda_{S,min}/5$  in the core, filter, fill regions, and PML. They are of primary interest for the analysis. In the foundation (apart from the PML), we allow an element size  $2\lambda_{S,min}/5$ , to reduce the number of elements. The total number of elements was  $4.6\cdot10^5$ . Measured by the skewness, the average element quality was 0.70 and the minimum quality 0.17. We consider the mesh quality good enough for the current study.

To validate that the results are independent of the mesh to a satisfactory degree, we present a grid sensitivity study in Appendix A. Appendix B presents a test of the dependency of the foundation size.

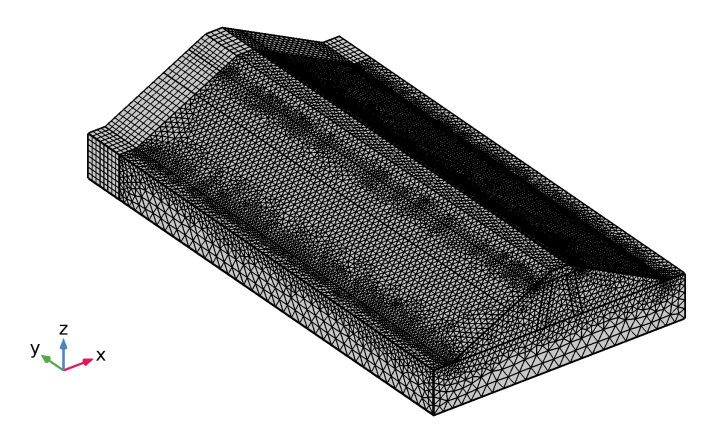


Figure 2 Illustration of the dam mesh used in the simulations.

#### 4.4 DEFECTS

Defects in real embankment dams can be imperfections in the original construction of the dam or be formed by internal erosion. If too severe, they can lead to a dam failure. We intended to model defects representing a core region where fines have been removed due to internal erosion. Lost fines are replaced by water, forming a more porous and permeable medium. This kind of defects could occur due to improperly designed filters. A photo of such a defect is shown in Figure 3. They can also create sinkholes, visible on the dam crest.





Figure 3 A cross-section of the dam at Lövön power plant during a dam reconstruction 1998. At the centre of the photographed region, the soil consists only of larger grains. Fines have been lost due to erosion. (Photo from Graningeverken AB.)

In the simulations, defects were assumed to be horizontal cylinders penetrating the core. Only one defect was considered per simulation, positioned with the centre at Section 50 m at a height 5 m above the foundation (i.e. y = 50 m and z = 5 m in Figure 1). The defect region was described by varying the material properties through a step function. Not changing the mesh when introducing the defects, the same mesh could be retained in all simulations. We used defect radii of  $r_d = 1$ , 2, and 4 m.

When lowering the porosity in a part of the core, the density is lowered, and the wave velocity is expected to increase correspondingly. Changes in the wave velocity are on the order of a few percentages, given in Table 1. The effect on the density by a defect of radius of 2 m is illustrated in Figure 4.

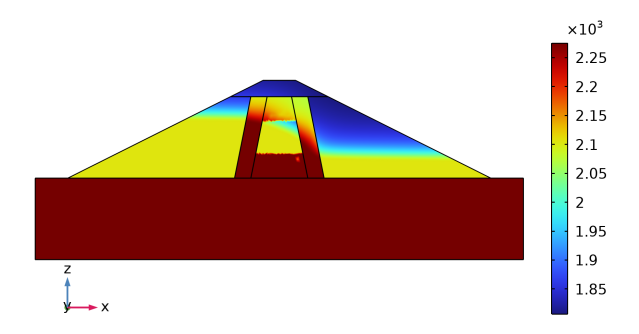


Figure 4 The density (kg/m³) at a cross-section of a dam with a core defect of radius 2 m, taken at the centre of the defect.



#### 5 Results

In this section, we discuss the simulation results. The results from the simulations of Richards' equation are shown first (Section 5.1). Thereafter, the analysis of the displacement vector is presented (Sections 5.2 and 5.3).

#### 5.1 VOLUME FRACTION, FLOW, AND PRESSURE FIELDS

As expected, the lower part of the dam and the foundation are almost fully saturated. In the top part of the dam, the volume fraction is  $\theta$  < 0.1. The liquid volume fraction and the density of the intact dam is shown in Figure 5.



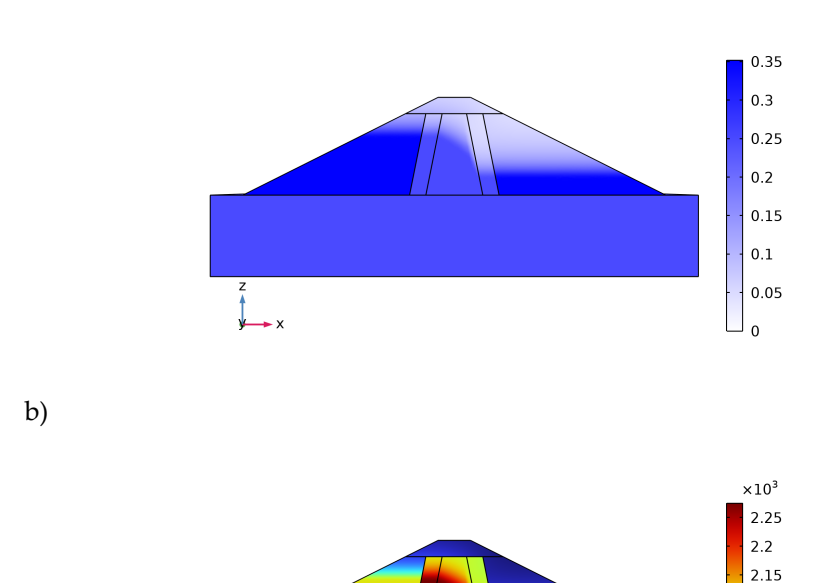


Figure 5 a) The liquid volume fraction and b) the effective density (kg/m³) of the intact dam.

The magnitude of the velocity field is shown in Figure 6a and streamlines in Figure 6b. The seepage velocities are typically on the order of 1–10  $\mu m/s$ . The flow can go through the foundation, but the velocities there are small. A minor flow also circumvents the core, going on top of it, because of capillary forces. We will not study this phenomenon closer here, and it is not believed to affect the results.

2.05

1.95 1.9 1.85



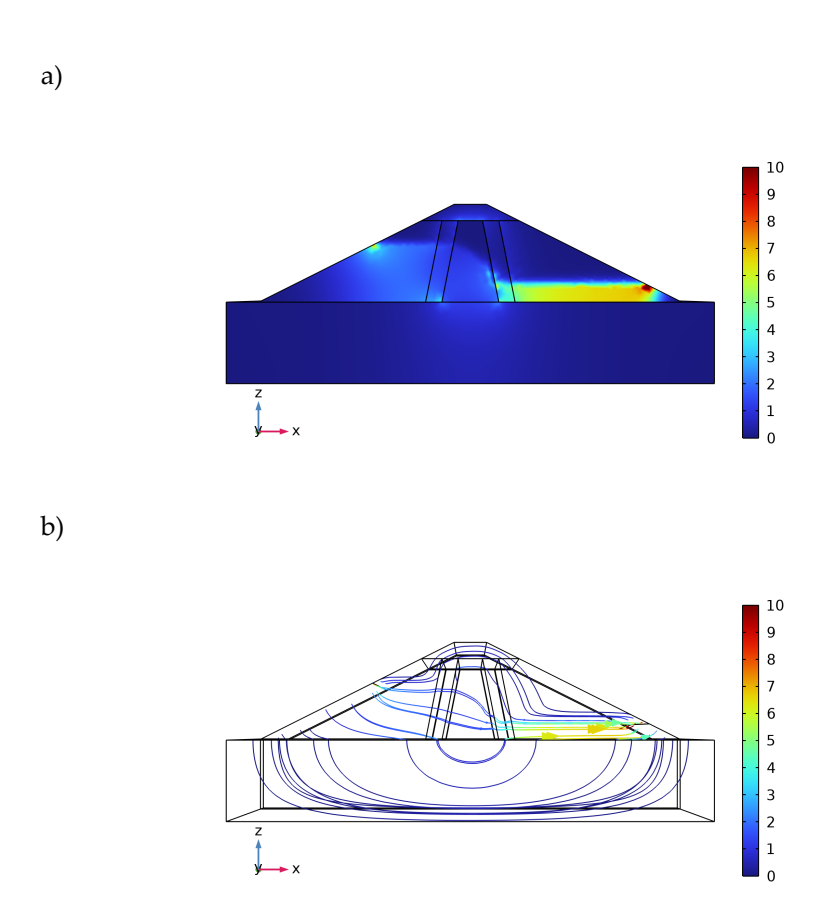


Figure 6 a) Velocity magnitude ( $\mu$ m/s) of the intact dam. The colour bar was limited to show 0-10  $\mu$ m/s. b) Streamlines, with arrowhead size and colour indicating velocity magnitude ( $\mu$ m/s).

At the top of the inlet and outlet, the flow needs to turn around corners. Fluid enters and exits the dam with the velocity parallel to the surface normal but must satisfy the impermeability condition directly above the water level. This change in flow direction gives rise to large velocities at the inlet and outlet edges. However, since these amplifications are local irregularities in the velocity field, they are not believed to affect the remaining analysis.

We computed the average seepage flow to 14 and 12 ml/(s·m) at the inlet and outlet, respectively, by integrating the boundary flux. These are typical values for Swedish dams. The PML was not included in these computations. The minor difference is due to numerical errors, which we believe do not affect the conclusions. The average flow rates with defects are shown in Figure 7, computed at the US and DS sides. It attains a value of around 200 ml/(s·m) for the largest defect (with  $r_d = 4$  m).



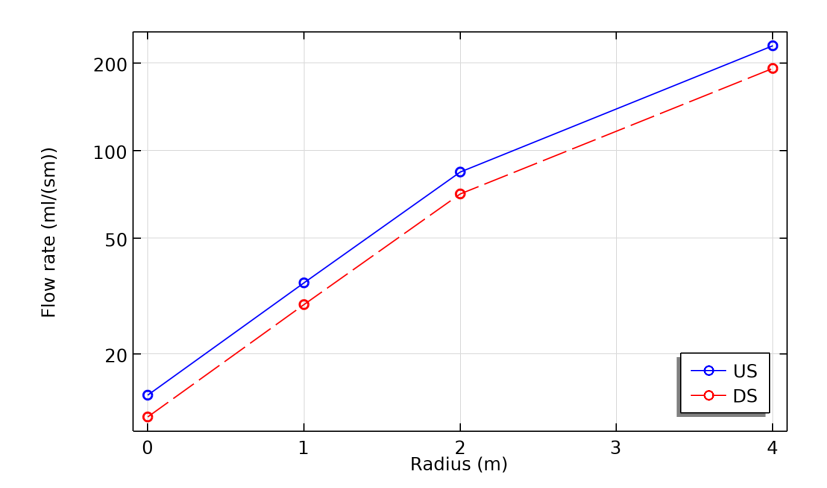


Figure 7 Average seepage flow rate as a function of the defect's radius. A radius of 0 m represents the intact dam. (Notice the logarithmic scaling on the vertical axis.)

The pressure field is shown in Figure 8. The pressure is lower on the DS than the US side at the same height, as the water level there is lower. The drop in pressure occurs mainly across the core. We show the water table ( $p_w = 0$ ) as a white line.

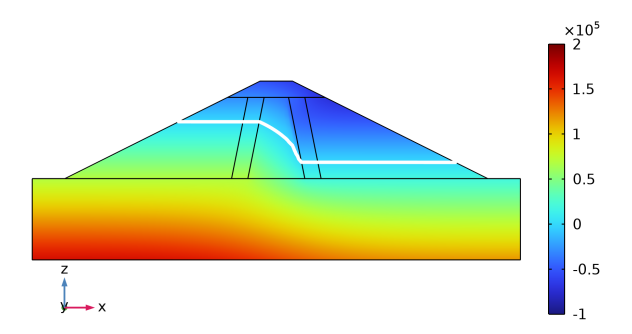


Figure 8 Dam pressure field (Pa) for the intact dam. Across the core, there is drop in pressure corresponding to the boundary conditions. The white line indicates the water table.

#### 5.2 STATIC LOAD

The effects of the static load are illustrated in Figure 9 by the linear elastic material (solid) pressure. This pressure equal one third of the negative trace of  $\sigma$ . It reaches a magnitude of about  $3\cdot 10^3$  Pa near the centre of the foundation. The values on the US side are slightly larger than on the DS side due to the higher water level there.



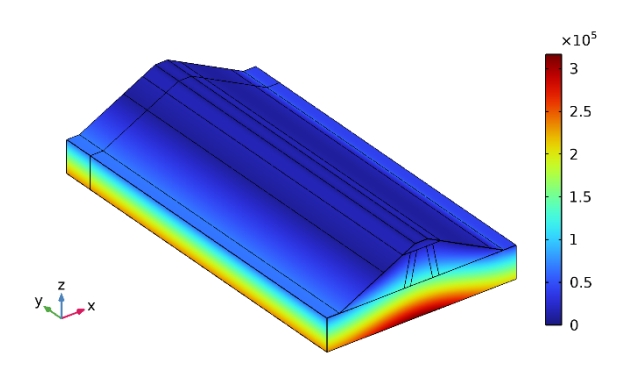


Figure 9 The linear elastic material pressure (Pa) due to static forces.

#### 5.3 FREQUENCY RESPONSE OF HARMONIC PERTURBATIONS

For ANI monitoring of infrastructure, a range of frequencies are of interest depending on the size of the asset and the expected extent of any defects. The range of investigation is often limited by the local ambient noise field. Waves with high frequencies provide higher resolution but are quickly attenuated. In industrial settings, noise sources with a particular frequency typically dominate the recorded wavefield, for example if a generator is functioning nearby. Johansson et al. (2022) were able to make use of frequencies in the range 15–27 Hz for monitoring and 10–25 Hz for imaging the Älvkarleby Test Dam.

For the modelling performed in this study, the harmonic perturbation consisted of a forcing at the edge of the dam crest. The force magnitude was 100 kN/m in the vertical direction (e.g. corresponding to the pressure force 10 kPa over 10 m) and the frequency was 15 Hz.

#### 5.3.1 Dam without defects

The vertical extent of the perturbation is illustrated in Figure 10. The harmonic perturbation gives rise to areas of higher and lower amplitude. The distance between two consecutive high-amplitude areas, corresponding to half a wavelength, compares well to the wavelength mentioned in Section 4.3.



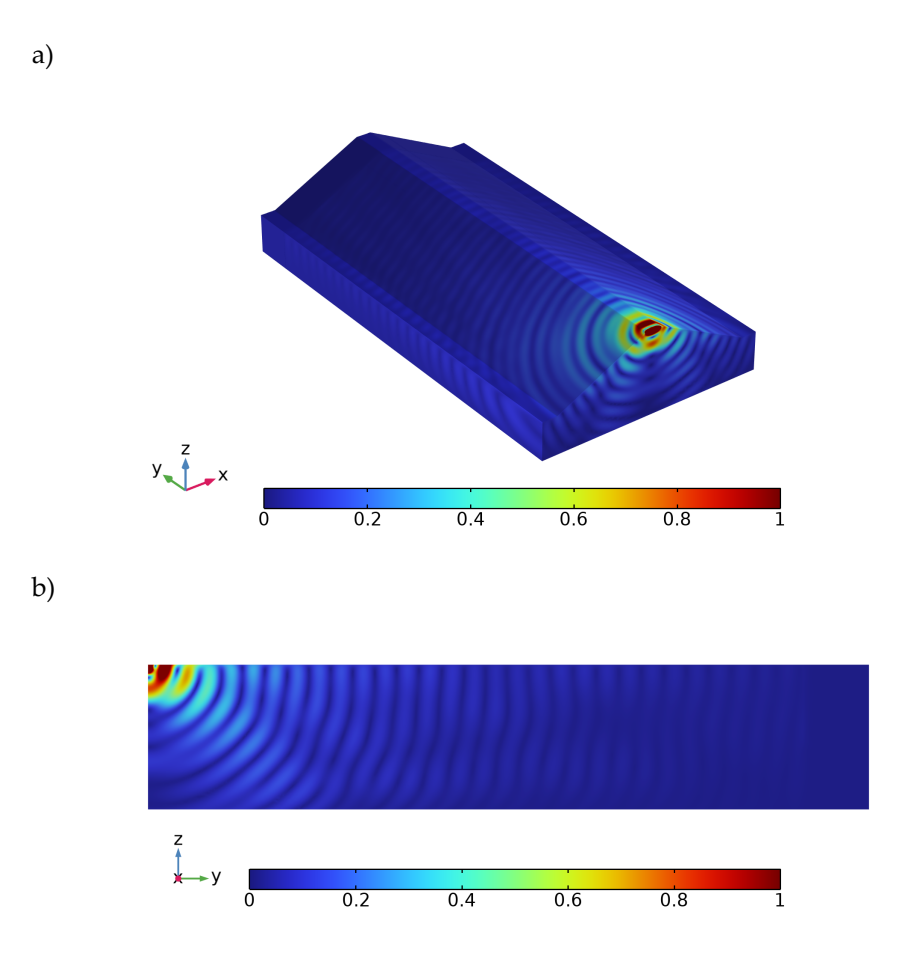


Figure 10 Displacement magnitude (mm) for the intact dam due to the harmonic forcing at a) the dam surface and b) a vertical slice at the crest centre. The PML region is also included.

As mentioned in Section 3.1, R-waves propagate with both parallel and transverse displacements. Therefore, we show the vertical and along-dam (spanwise) displacements ( $s_z$  and  $s_y$ , respectively) at a vertical cross-section along the crest (Figure 11). Both displacement fields show clear wave patterns. The magnitude of  $s_z$  is generally larger than  $s_y$ . There are also waves not travelling along the dam crest. They are of less interest here.



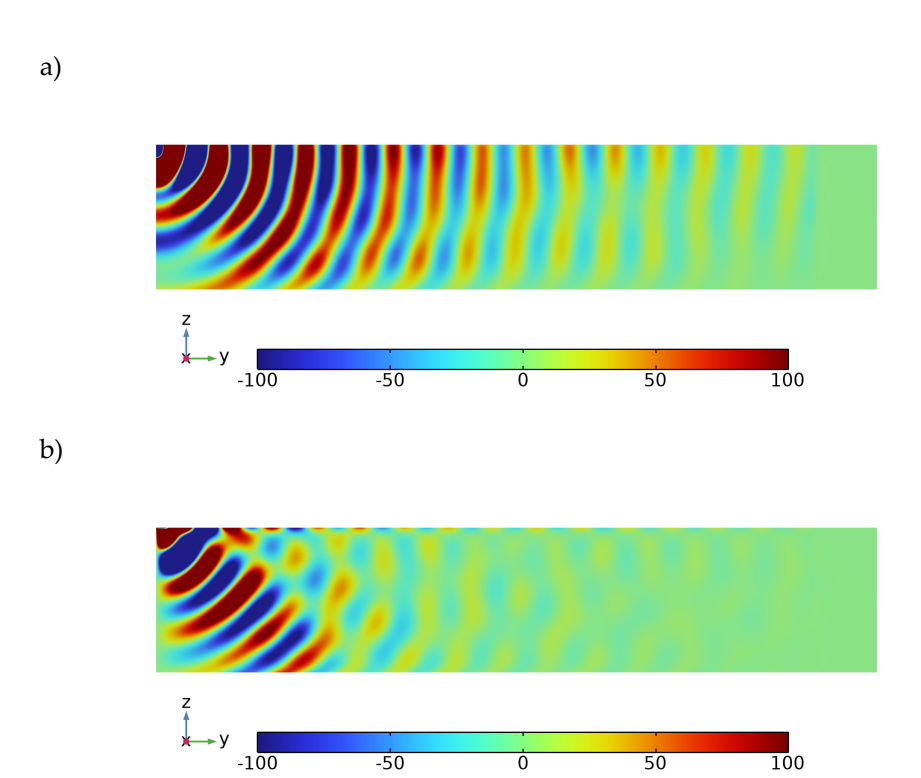


Figure 11 a) Vertical and b) spanwise displacement fields ( $s_z$  and  $s_y$ , in  $\mu m$ ) at a vertical slice at the crest centre.

The spanwise displacement has a change in sign close to the crest. We illustrate this phase shift in Figure 12, where we show  $s_y$  and the absolute value of  $s_z$  at Sections 51 and 79 m at different depths. The spanwise displacement changes sign at a depth of around 1 m. Even if this distance corresponds to about one mesh element, the sign shift is still captured in the simulations. R-waves typically have this shift at a depth of about  $0.2\lambda$ , but the exact value depends on the Poisson's ratio (Richart, Hall, & Woods, 1970, p. 89).

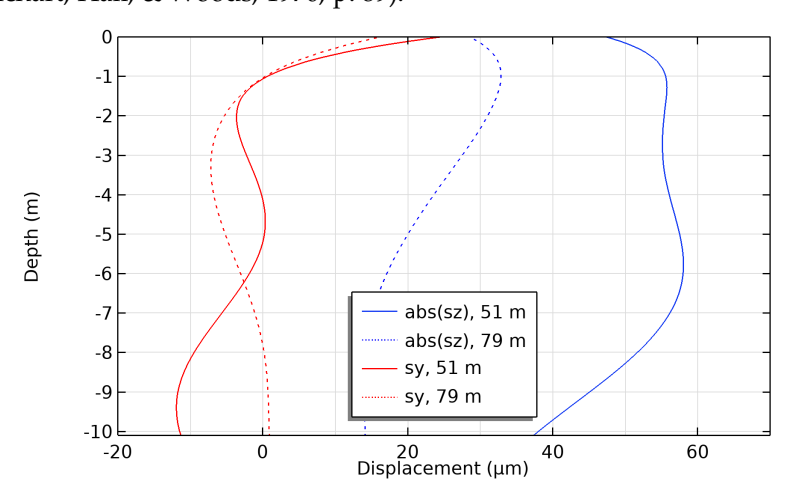


Figure 12 Vertical and spanwise displacements ( $s_z$  and  $s_y$ , respectively) at Sections 51 and 79 m. The depth corresponds to z -  $z_{crest}$ , where  $z_{crest}$  is the location of the dam crest. Only the absolute value of the (complex) vertical displacement is shown, whereas the phase is included for the horizontal displacement to illustrate the shift in sign around a depth of 1 m.



Apart from the sign change, the displacement depth dependency at 51 m appears somewhat atypical; the displacement caused by R-waves is expected to decay to zero over a depth on the order of one wavelength. At 79 m, the decay is more ordinary. We performed tests with defects at different sections (Appendix C). The general behaviour did not change, even if the magnitude of the effect of the defect varied somewhat. The dam geometry and interference with P- or S-waves can affect R-wave recordings (Richart, Hall, & Woods, 1970, p. 89; Bièvre, et al., 2017). In media with depth-dependent properties, several surface wave modes may also form (Socco, Foti, & Boiero, 2010).

We considered an artificial optical fibre "crest cable" placed at the core crest centre. A similar crest cable was used for measurements by Johansson et al. (2021; 2022). The vertical displacement due to the perturbation at the crest cable is shown in Figure 13. We show both the absolute value of the (complex) vertical displacement and its phase. The absolute value decays almost monotonically with increasing distance from the source and the phase show a linear variation with section.

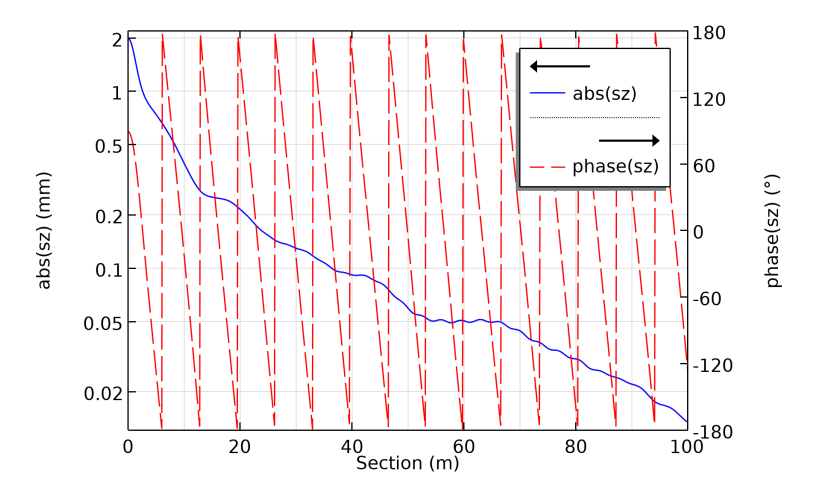


Figure 13 Vertical displacement due to the perturbation at crest cable, showing absolute value and phase (left and right vertical axis, respectively). The left vertical axis has a logarithmic scaling.

#### 5.3.2 Defects' effect on phase velocity

The absolute value and the phase of the vertical displacement are shown in Figure 14 for the dam with and without defects. The absolute value is hardly affected by the defects. However, there is a small phase shift introduced at the defects around Section 50 m, visible at least for the largest defect ( $r_d$  = 4 m).



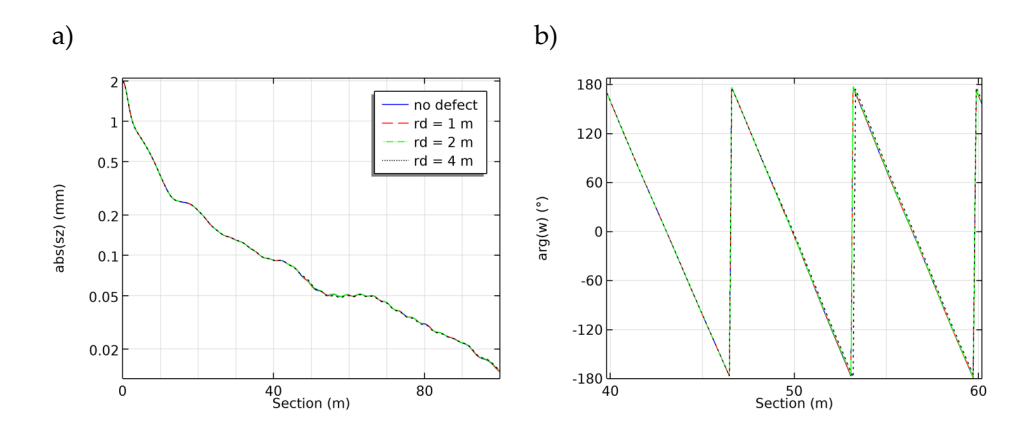


Figure 14 Cable vertical perturbation displacement, with and without a defect of radius  $r_d$ , showing a) the absolute value and b) the phase in the region around the defect. The legend in (a) also applies to (b).

The wave phase velocity can be computed from the displacement field phase. The frequency is assumed to be equal to that of the perturbation. It is assumed that it has a harmonic variation  $e^{i2\pi f}$  in complex notation (where the real part is the actual perturbation and  $i=\sqrt{-1}$ ). Correspondingly, we describe a wave propagating along the dam (i.e. in the *y*-direction) by assuming

$$s_z = |s_z|e^{i\xi} = |s_z|e^{i(2\pi ft - ky + const.)},$$
 (20)

where  $\xi$  is the phase, k is the wavenumber, and *const.* indicates a constant (COMSOL AB, 2022a, p. 436). The wave phase velocity is

$$V = \frac{2\pi f}{k} = -\frac{2\pi f}{\partial \xi / \partial \gamma}.$$
 (21)

This formula was used to compute the wave velocity from the simulation results, shown in Figure 15a. It is around 100 m/s, agreeing well with the predictions in Table 1.

The velocity differences that the defects generate are around 0.5–3%, shown in Figure 15b. These differences are on the same order of magnitude as those indicated in Table 1, comparing core and defect velocities. However, the defects only cover a small region of the dam cross-section, explaining why the effective velocity differences appear smaller than the theoretical predictions. Figure 15b also show that the magnitude of the velocity difference is reduced with defect size. The precision of the measurement equipment can be expected to determine the smallest defect size visible in practice for a given wavelength.

Velocity fluctuations on the order of 5 m/s are present also for the intact dam. In the proximity of the source, the surface wave has not fully developed, and we cannot expect a constant velocity. However, the fluctuations are present also at larger *y*-coordinates. Simulation results from an extended dam suggested that the dam end boundary condition (i.e. the PML) was involved in their formation (Appendix C). Changing the foundation material also reduced their magnitude (Appendix E). Influence of dam ends and the foundation, e.g. by interference from reflected waves, are unavoidable in practice and must be handled in real dams.



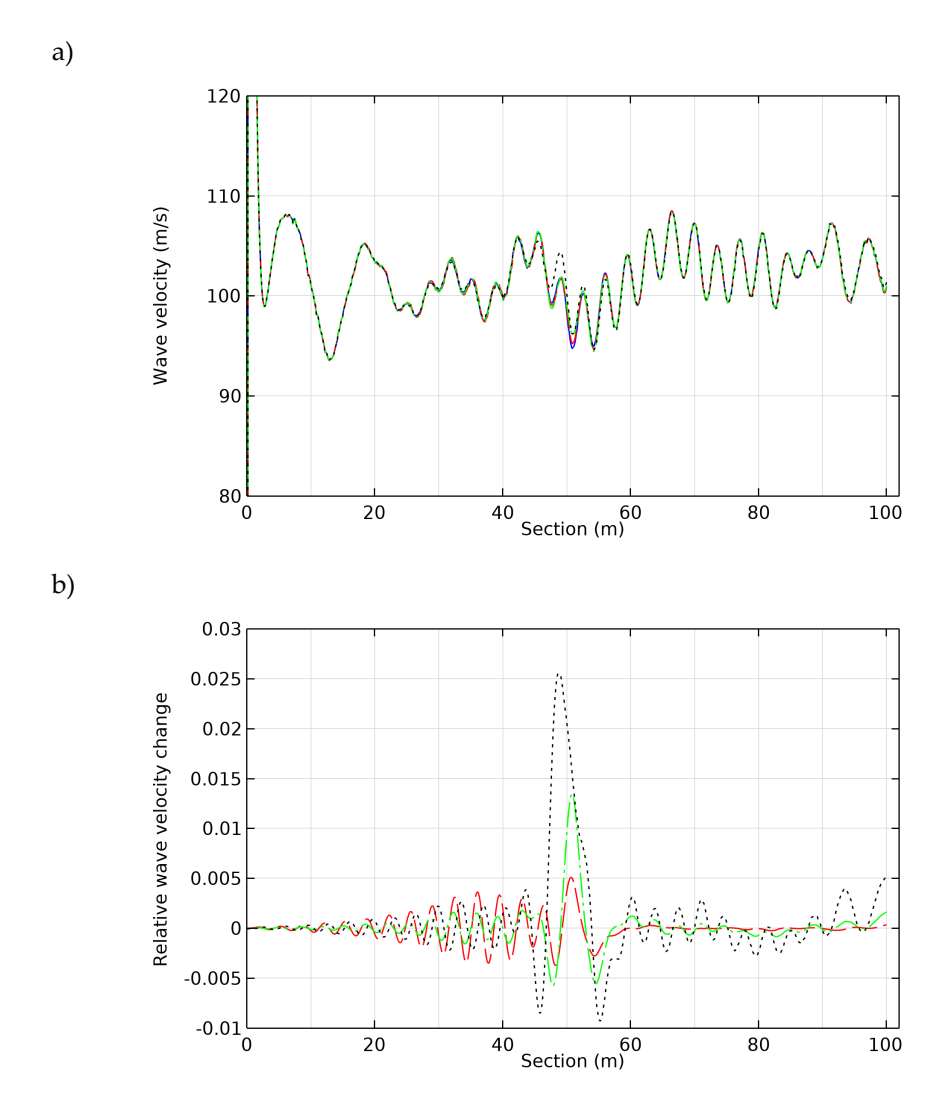


Figure 15 a) Wave phase velocity, computed from the vertical displacement perturbation phase, and b) relative wave phase velocity change compared to the dam without defects. The line styles (and colours) are the same as in Figure 14a.

The largest velocity deviations occur around the centre of the defects at Section 50 m. The defects could be expected to be located at the largest deviations and would thereby be correctly identified. There are also smaller differences before and after this region. We expect that reflections and refracted waves due to the change in material properties causes these fluctuations. In a dam with an unknown number of defects, they could make it difficult to identify smaller defects. However, if material properties changed more gradually, it is possible that these fluctuations would be reduced.

Studies of the impact of US water level and foundation type are given in Appendices D and E, respectively. The impact of water level appears to be minor for the current parameters. Changing the porosity of the foundation to 2% (resembling rock) dampened velocity oscillations away from the source. It also lowered the velocity difference due to the defect slightly.



#### 6 Conclusions and outlook

Inhomogeneities in embankment dams and their foundations can be identified with seismic waves as they change the wave velocity. We have performed simulations of a generic embankment dam with a defect region and analysed the wave velocity difference compared to an intact dam. The defect was assumed to be a horizontal cylindrical region with higher porosity in the core. Such defects could be caused by internal erosion.

The liquid volume fraction of the dam was found by solving Richards' equation. The volume fraction was then used to compute an effective material density. In the seismic wave simulations, the dam was assumed to be a linear elastic medium. The higher porosity in the defect region implies a lower density, increasing the wave velocity. We used a harmonic vertical force with a frequency of 15 Hz as noise source, exciting surface waves travelling along the dam crest.

At realistic porosities, the velocity deviations due to the defects were on the order of 1%. In the simulations of the intact dam, the computed wave velocity had fluctuations larger than this value. They might be caused by reflections induced at the dam end boundary or by variations in geometry and material properties with depth. Such fluctuations are expected to exist also in real dams. However, looking at the maximum difference in wave speed compared to the intact dam, the defect dam section could be correctly identified.

Given careful analysis, Ambient Noise Interferometry (ANI) can reliably detect changes in velocity of less than 0.5%. Therefore, the simulations indicate that this monitoring technique could be applicable to dams. Such optical-fibre based seismic methods are easy to implement since many dams have optical fibres installed already. The potential of optical-fibre methods is also a compelling reason to install optical fibres when constructing new dams. We believe that ANI could be suitable for both monitoring and investigations of dams.

As a continuation of this study, we propose performing simulations of waves at different frequencies and investigating how they are influenced by defects at different depths. Abutments and wider geology could also be incorporated in the simulation geometry. Finally, we suggest carrying out simulations of experimental setups (e.g. the Älvkarleby Test Dam), enabling a direct comparison between simulation and experimental results.

COMSOL Multiphysics and COMSOL are registered trademarks of COMSOL AB.



#### 7 References

- Bièvre, G., Lacroix, P., Oxarango, L., Goutaland, D., Monnot, G., & Fargier, Y. (2017). Integration of geotechnical and geophysical techniques for the characterization of a small earth-filled canal dyke and the localization of water leakage. *Appl. Geophys.*, 139, 1–15.
- Biot, M. A. (1956a). Theory of Propagation of Elastic Waves in a Fluid-Saturated Porous Solid. I. Low-Frequency Range. *J. Acoust. Soc. Am.*, 28, 168–178.
- Biot, M. A. (1956b). Theory of propagation of elastic waves in a fluid-saturated porous solid. II. Higher frequency range. *J. Acoust. Soc. Am.*, 28, 179–191.
- Bishop. (1960). The principle of effective stress. *Norwegian Geotechnical Institute Publication No.* 32, 1–5.
- Cho, G. C., & Santamarina, J. C. (2001). Unsaturated particulate materials—particle-level studies. *J. Geotech. Geoenvironmental Eng.*, 127, 84–96.
- COMSOL AB. (2022a). Structural Mechanics Module User's Guide. COMSOL Multiphysics® v. 6.1. Stockholm, Sweden.
- COMSOL AB. (2022b). Subsurface Flow Module User's Guide. COMSOL Multiphysics® v. 6.1. Stockholm, Sweden.
- COMSOL AB. (2022c). *Acoustics Module User's Guide. COMSOL Multiphysics*® v. 6.1. Stockholm, Sweden.
- Dong, Y., & Lu, N. (2016). Dependencies of shear wave velocity and shear modulus of soil on saturation. *J. Eng. Mech.*, 142, 04016083.
- Gassmann, F. (1951). Über die Elastizität poröser Medien. Vierteljahrsschrift der Naturf. Gesellschaft in Zürich, 96, 1–23.
- Hardin, B. O., & Black, W. L. (1968). Vibration modulus of normally consolidated clay. *J. Soil Mech. Found. Div.*, 94, 353–369.
- Johansson, S., & Sjödahl, P. (2017). Fibre-optic temperature monitoring for seepage detection in embankment and tailings dams. 85th Annu. Meeting of the Intern. Commission on Large Dams.
- Johansson, S., & Watley, D. (2006). Distributed sensing of seepage and movements using optical fibres some results from innovative installations in embankment dams in Sweden. *ICOLD Congress* 2006, Q. 84 R. 69.
- Johansson, S., Beaupretre, S., Boue, A., & Stork, A. (2021). *Distributed Acoustic Sensing* for Detection of Defects in the Test Dam at Älvkarleby. Energiforsk, Report 2021:732, ISBN 978-91-7673-732-3.
- Johansson, S., Beaupretre, S., Mordet, A., & Stork, A. (2022). *Distributed Acoustic Sensing* for Detection of Defects in the Test Dam at Älvkarleby Phase 2. Energiforsk, Report 2022:874, ISBN 978-91-7673-874-0.
- Ju, S.-H., & Ni, S.-H. (2007). Determining Rayleigh damping parameters of soils for finite element analysis. *Int. J. Numer. Anal. Meth. Geomech.*, *31*, 1239–1255.
- Malischewsky, P. G. (2005). Comparison of approximated solutions for the phase velocity of Rayleigh waves (Comment on 'Characterization of surface damage via surface acoustic waves'). *Nanotechnology*, *16*, 995–996.
- Mitchell, J. K., & Soga, K. (2005). Fundamentals of Soil Behavior. John Wiley & Sons, Inc.
- Ng, C. W., Zhou, C., & Chiu, C. F. (2020). Constitutive modelling of state-dependent behaviour of unsaturated soils: an overview. *Acta Geotech.*, *15*, 2705–2725.
- Park, C. B., Miller, R. D., & Xia, J. (1999). Multichannel analysis of surface waves. *Geophysics*, 64, 800–808.



- Parker, T. R., Farhadiroushan, M., Handerek, V. A., & Roger, A. J. (1997). A fully distributed simultaneous strain and temperature sensor using spontaneous Brillouin backscatter. *IEEE Photon. Technol. Lett.*, *9*, 979–981.
- Parker, T., Shatalin, S., & Farhadiroushan, M. (2014). Distributed Acoustic Sensing a new tool for seismic applications. *First Break*, 32, 61–69.
- Richart, F. E., Hall, J. R., & Woods, R. D. (1970). *Vibrations of Soils and Foundations*. Prentice-Hall, Inc.
- Santamarina, J. C., Klein, K. A., & Fam, M. A. (2001). Soils and Waves. J. Wiley & Sons.
- Sjödahl, P., Johansson, S., & Dahlin, T. (2019). *Geofysiska metoder inom dammsäkerhetsområdet: En kunskapssammanställning*. Energiforsk, Report 2019:571, ISBN 978-91-7673-571-8.
- Socco, L. V., Foti, S., & Boiero, D. (2010). Surface-wave analysis for building near-surface velocity models—Established approaches and new perspectives. *Geophysics*, 75, 75A83–75A102.
- Terzaghi, K. (1936). The shearing resistance of saturated soils and the angle between the planes of shear. *Proc. of the First Intern. Conf. on Soil Mechanics, 1,* 54–56.
- Vahedifard, F., Thota, S. K., Cao, T. D., Samarakoon, R. A., & McCartney, J. S. (2020). Temperature-dependent model for small-strain shear modulus of unsaturated soils. *J. Geotech. Geoenviron. Eng.*, 146, 04020136.
- van Genuchten, M. T. (1980). A closed-form equation for predicting the hydraulic conductivity of unsaturated soils. *Soil. Sci. Soc. Am. J.*, 44, 892–898.



# Appendix A: Mesh sensitivity study

To test the sensitivity of the results to the mesh, we performed simulations with two other grids. One grind had maximum element size  $2\lambda s_{,min}/5$  everywhere, including the PML (grid 2). Its PML was resized to 20 m to fit eight mesh layers. The other grid had a refined mesh in the core, filter, and the support fill closest to the crest (grid 3). The maximum element size in those regions was  $0.75 \cdot \lambda s_{,min}/5$ . In the PML, the maximum element size was  $\lambda s_{,min}/5$  and elsewhere  $2\lambda s_{,min}/5$ . The grid described in Section 4.3 is referred to as grid 1.

We performed simulations of the intact dam and with a defect radius  $r_d$  = 2 m with grid 2 and 3. The average seepage flow rate is reported in Table 2, computed on the US side. Grid 2 gives the lowest seepage flow. The differences are around 5%, which is irrelevant for the conclusions of this report.

Table 2 Average seepage flow rate for the different grids (PML not included).

		Radius 2 m $[ml/(s \cdot m)]$
Grid 1 Grid 2 Grid 3	14.4	84.4
Grid 2	13.7	81.1
Grid 3	14.4	83.7

The computed wave speed is shown in Figure 16a for the intact dam, and the velocity difference is shown in Figure 16b. There is a satisfactory agreement between the different grids, indicating that the seismic simulation results are independent of the mesh to a tolerable degree. Therefore, grid 1 is suitable for the current simulation parameters. Grid 2 give rise to more noise than grid 1 because of its lower resolution.



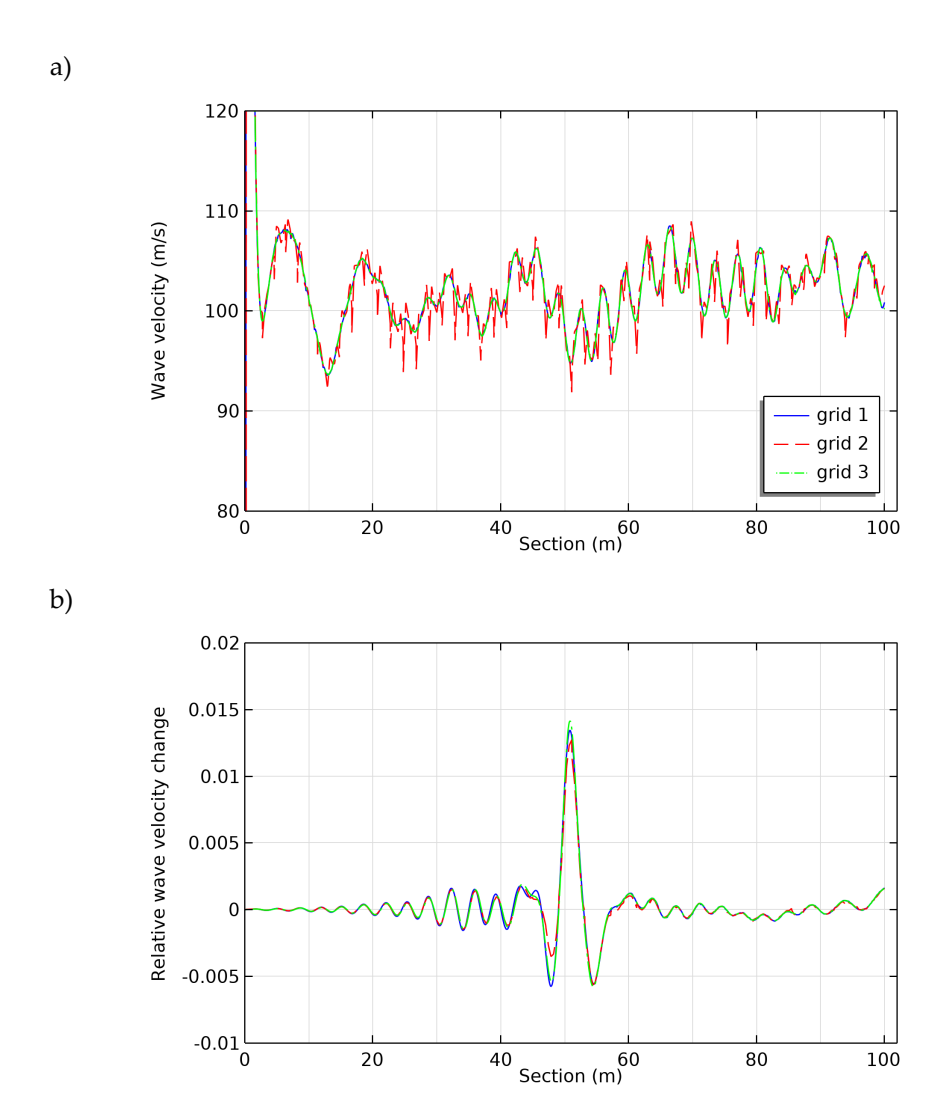


Figure 16 a) Wave phase velocity for the intact dam and b) the relative wave velocity difference for the dam with a defect with  $r_d = 2$  m. The line styles in (b) are the same as in (a).



# **Appendix B: Foundation size sensitivity study**

To test the sensitivity of the results to the foundation dimensions, we performed a simulation with its size extended. The depth was increased from 10 to 20 m and the extrusion of the foundation beyond the side fills on the US and DS sides was extended from 4 to 8 m. The new geometry is shown in Figure 17. The dam had no defects, and we used a grid with settings corresponding to grid 2. It resulted in an average seepage flow rate on the US side of 15.7 ml/(sm). This value is higher than those reported in Table 2. The increase is likely caused by the larger seepage area created by the larger foundation. However, the change is relatively minor.

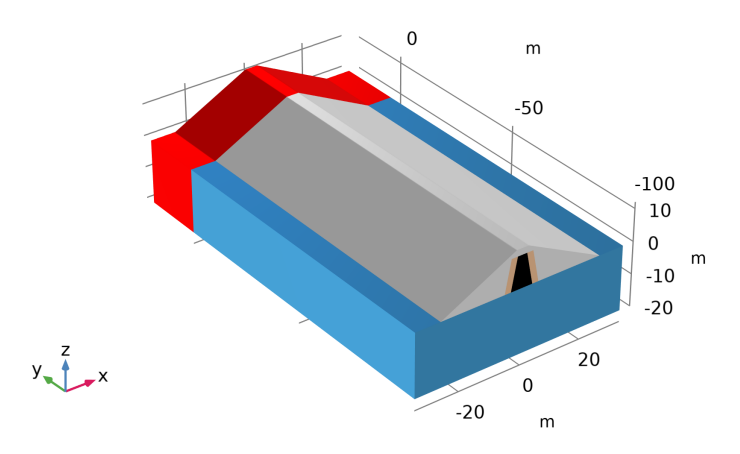


Figure 17 Dam with extended foundation. The colours are the same as in Figure 1.

The computed wave velocity is shown in Figure 18. The change in wave velocity due to the domain enlargement is small enough to be neglected for the current study.

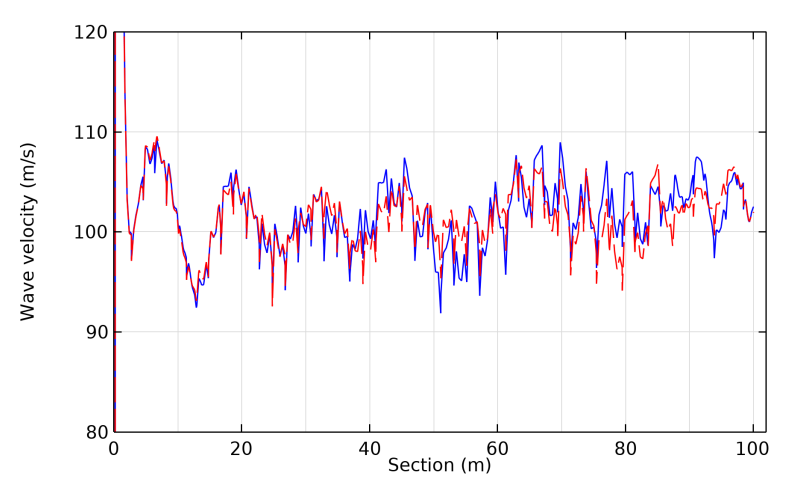


Figure 18 Wave phase velocity for the intact dam, computed with the regular and an extended domain.



# Appendix C: Effects of defect spanwise location

To see the effects of the spanwise location of the defect, we performed a simulation with the defect centre location moved to Section 75 m, using  $r_d$  = 2 m. This close to the edge of the dam, boundary conditions could affect the flow related to the defect to a higher extent. However, it is probable that S- and P-waves have been reduced to a higher extent at this section because of geometric spreading. Still, reflection can affect the details of the result.

The average seepage flow rate (on the US side) was computed to 83.4 ml/(sm) for the new location. It is slightly lower than the value reported in Table 2. However, the difference is not significant.

The velocity difference between the intact and defect dams is shown in Figure 19 for both the original and the new defect location (solid and dashed lines, respectively). The maximum difference is located close to the centre of the defect in both setups. However, the magnitude of the difference has changed from about 1.3% to 0.6%. It shows that the defect location affects the wave velocity.

Due to this relatively large change, we performed simulations with a longer dam, using mesh settings corresponding to grid 2 (cf. Appendix A). This dam had the length extended from 100 m to 200 m (however the same PML dimensions). We performed seven simulations of the new dam: without defect and with one defect (at sections 50, 75, 100, 125, 150, or 175 m). The results are also shown in Figure 19. The simulations with a defect at 50 and 75 m gave results that agreed well with the shorter dam results. There is no clear trend in how the velocity difference depends on the spanwise location. The minimum is found for 75 m and the maximum for 150 m (2.0%).

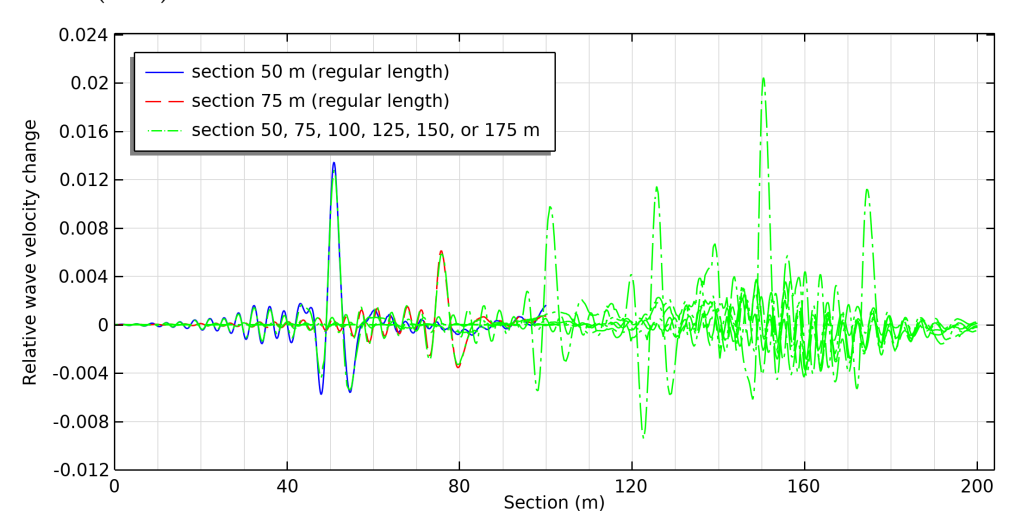


Figure 19 The relative velocity difference due to a dam defect with  $r_d$  = 2 m for the regular 100 m dam and a 200 m dam. The defect has been placed at different sections, indicated by the legend. All line styles are the same for the long dam results, for simplicity.

We also show the wave velocity for the long and shorter intact dams in Figure 20 (for grid 2). They agree well. However, the velocity oscillations on the order of 5



m/s seem to have moved as the dam was extended. This change is an indication that the dam end boundary condition is the source of these fluctuations.

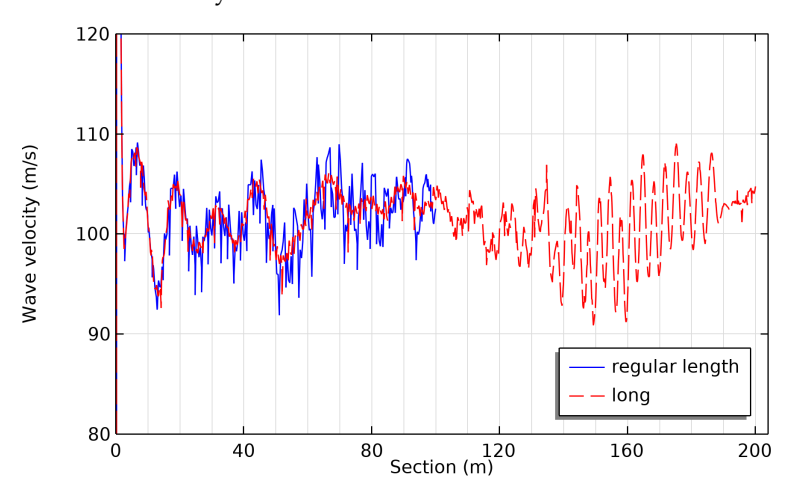


Figure 20 Wave phase velocity for the intact dam, computed with the regular and long domain.



# Appendix D: Water level dependency

The US water level determine the water content at the defect. To test the dependency on this parameter, it was changed from  $z_{WL,US} = 7$  to 5 and 3 m. In these simulations, the defect with  $r_d = 1$  m was used. The three  $z_{WL,US}$  correspond to an US water level above, at, and below the defect centre at z = 5.

In Figure 21, we show the computed velocity for the different water levels of the intact dam. The velocity tends to be higher the lower the water level, reflecting the decrease in density. It is possible that neglected capillary and stress effects on the shear modulus would give rise to larger changes (Section 3.2).

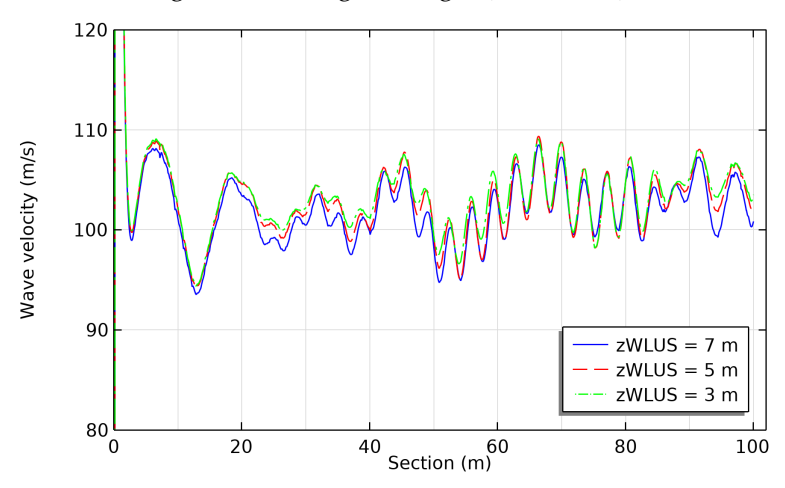


Figure 21 Wave velocity for the intact dam at different US water levels.

The velocity differences between the intact and defect dams are shown in Figure 22. The magnitude of the difference is only slightly affected. The minor velocity variations in Figure 21 indicate that the wavelength only varies marginally with water level, which could explain the small difference. Interestingly, the smallest maximum is achieved for the intermediate water level. For this *zwl.us*, the maximum is actually not achieved at the location of the defect but at Section 36 m.



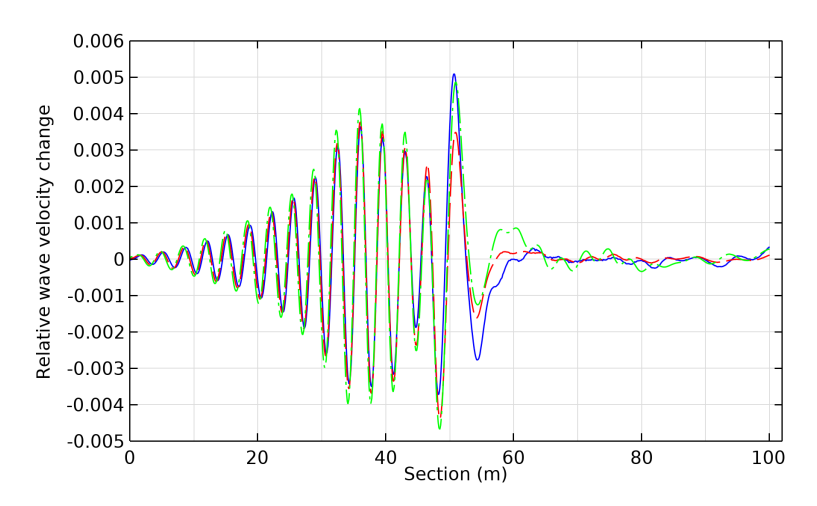


Figure 22 Wave velocity differences between intact and defect dams for a defect radius  $r_d = 1$  m and different US water levels. The line styles are the same as in Figure 21.



# Appendix E: Dam on rock foundation

Setting the porosity in the foundation equal to that of the core implies that the foundation is made of till or similar. We performed a simulation with the porosity of the foundation lowered to 2%, corresponding to rock. The permeability and the grid were kept the same.

The computed wave velocities of intact dams with till and rock foundations are shown in Figure 23. The velocity oscillations away from the source are slightly smaller for the dam with the heavier rock foundation.

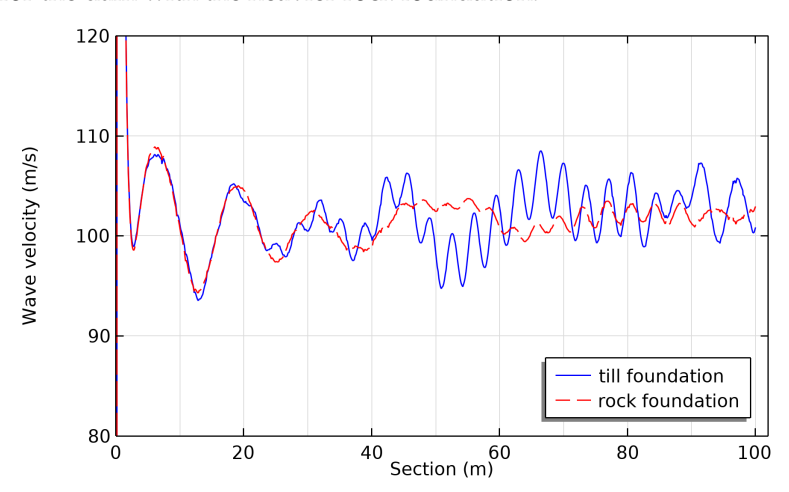


Figure 23 Wave velocities of intact dams with different foundation porosity.

The velocity differences between intact and defect dams are given in Figure 24 for defects with radius  $r_d = 2$  m. The rock foundation has reduced the impact of the defect. However, the overall behaviour is similar for the two foundation types.

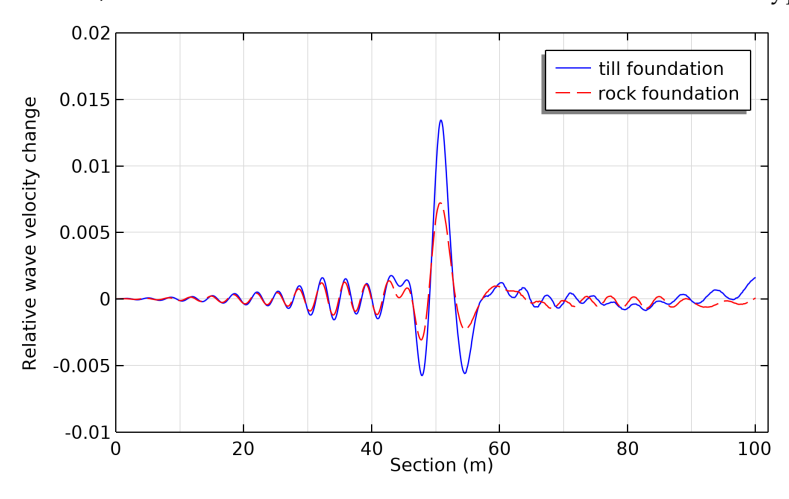


Figure 24 Wave velocity differences between the intact and defect dams for  $r_d$  = 2 m. The line styles are the same as in Figure 23.



# SIMULATING SEISMIC WAVES IN EMBANKMENT DAMS FOR OPTICAL FIBRE DISTRIBUTED ACOUSTIC SENSING

Akustiska metoder för övervakning eller undersökning kan effektivt tillämpas på fyllningsdammar med optiska fibrer installerade. Dessa metoder är baserade på seismiska vågors egenskaper, i synnerhet hastighet, vilken kan mätas i den optiska fibern. Numeriska simuleringar kan kvantifiera skillnader i våghastighet mellan en intakt damm och en damm med en lokal defekt. Simuleringarna i denna studie använder finita elementmetoden och undersöker effekterna av en defekt som skulle kunna ha orsakats av inre erosion. De hastighetskillnader som syns är tillräckligt stora för att registreras av moderna instrument. Modellen visar också att förändringar inte heller behöver ske i direkt anslutning till mätpunkten för att upptäckas. Akustiska metoder skulle kunna komplettera mer etablerade övervakningsmetoder som temperaturmätningar i optisk fiber.

Vi gör energivärlden smartare!

Genom samarbete och dialog bedriver vi energiforskning så att ny kunskap skapar värde för näringsliv, kunder och samhället i stort. Vi är det naturliga navet i energiforskningen – en opartisk aktör till nytta för framtidens energisystem.

